

Laue pattern analysis for two-dimensional strain mapping in light-ion-implanted polycrystals

Mona Ibrahim, É. Castelier, H. Palancher, Michel Bornert, Sabine Caré, J.-S. Micha

▶ **To cite this version:**

Mona Ibrahim, É. Castelier, H. Palancher, Michel Bornert, Sabine Caré, et al.. Laue pattern analysis for two-dimensional strain mapping in light-ion-implanted polycrystals. Journal of Applied Crystallography, 2015, 48 (4), pp.990-999. 10.1107/S1600576715007736 . hal-01248717

HAL Id: hal-01248717
https://enpc.hal.science/hal-01248717

Submitted on 24 Apr 2019

HAL is a multi-disciplinary open access archive for the deposit and dissemination of scientific research documents, whether they are published or not. The documents may come from teaching and research institutions in France or abroad, or from public or private research centers.

L'archive ouverte pluridisciplinaire **HAL**, est destinée au dépôt et à la diffusion de documents scientifiques de niveau recherche, publiés ou non, émanant des établissements d'enseignement et de recherche français ou étrangers, des laboratoires publics ou privés.

Laue pattern analysis for 2D strain mapping in light ion implanted polycrystals

M. Ibrahim,[a,b] É. Castelier,[a]* H. Palancher,[a] M. Bornert,[b] S. Caré[b] and J.-S. Micha[c]

[a] *CEA, DEN, DEC, Centre de Cadarache, 13 108 St Paul lez Durance, France,* [b] *Laboratoire Navier, Université Paris Est, UMR CNRS/IFSTTAR/ENPC, 77455 Marne-la-Vallée, France, and* [c] *CEA, INAC, 38 054 Grenoble Cedex 9 , France.*

E-mail: etienne.castelier@cea.fr

Abstract

In polycrystals implanted by light ions, a thin layer close to the surface is deformed. X-ray micro-diffraction in Laue mode is used to measure the induced strain. In the resulting Laue patterns, the diffraction spots are observed to split forming double spots, one corresponding to the non-deformed substrate and the other to the deformed layer. A specific image analysis, using bi-Gaussian shape functions, has been developed to improve diffraction spots detection. This is used in association with several numerical tools (conditioning, goodness-of-fit, hat matrix, etc.), based on least squares techniques and statistics, for detecting incorrect data and estimating the accuracy of the result. The use of these tools is not restricted to the study of ion implanted polycrystals but should find a systematic application for strain analysis from Laue patterns.

1. Introduction

Light ion implantations in materials has been used for both fundamental studies and technological purposes. Hence, the behaviour of both the implanted element (diffusion, precipitation, etc. (Garcia *et al.*, 2012)) and the damaged matrix has been widely studied. It has been recently shown that Laue diffraction using micro focused X-ray beams (μ-XRD) could be a powerful technique for probing strains induced by light ion implantation in polycrystals (Richard *et al.*, 2012). Synchrotron generated X-ray beam, smaller than the implanted polycrystal grain size, enables the characterisation of intragranular strains. The X-ray energies are often high enough to probe both the implanted layer and the non-implanted part of the grain (i.e. substrate). As a consequence, μ-XRD Laue patterns exhibit the contributions on the same crystal of both the strained and the strain-free material: each diffraction spot is double. This type of pattern is used for an accurate strain analysis in the implanted layer, relative to the substrate.

For about 15 years, Laue micro XRD has been applied for determining grain orientation and local strain in polycrystals (Tamura *et al.*, 2002; Barabash *et al.*, 2009; Villanova *et al.*, 2012; Marichal *et al.*, 2013; Liu *et al.*, 2014). See Barabash and Ice (Barabash & Ice, 2014) for a recent review. Software suites (e.g. XMAS (Tamura *et al.*, 2003), LaueTools (Micha, 2012)) allow the automatic analysis of such Laue patterns. However, these tools cannot be directly used for patterns collected on implanted polycrystals because of the overlap of the spots coming from the substrate and the deformed layer. Therefore, image analysis methods need to be adapted to this special case of Laue patterns. More details about the specificities of Laue patterns measured on implanted samples are given in section 2.2.

In a previous work (Richard *et al.*, 2012), a digital image analysis methodology has been proposed for estimating the strain of the implanted layer in UO_2 polycrystals

implanted with Helium ions at 60 keV. Despite its limits, the results were validated by a mechanical model, which explains the layer deformation by a swelling induced by the He implantation. The swelling rate estimated from this model has been found to be approximately the same as the one measured on aged UO_2 pellets enriched with short life α-emitter (Richard *et al.*, 2014). Although these methods have been validated for measuring the strain field within grains, they still have to be improved for exploring the intragranular variations which are usually small. The current paper presents therefore the development of more accurate image analysis procedures and of new tools for examining the quality of the refined strain tensor.

After describing the implanted polycrystals and the micro-diffraction experimental setup used here, the main challenges related to this image analysis are listed. The improved image analysis, and several tools (i.e. filters) for controlling the least square fitting of the strain tensor are then presented. Finally the efficiency of this methodology for intragranular strain mapping is evaluated on diffraction data measured on 60 keV He implanted polycrystals.

2. Laue micro XRD on implanted UO_2 polycrystals

The UO_2 sample preparation, the strain field induced by He implantation, and the resulting Laue patterns, obtained by X-ray micro-diffraction, have already been presented in previous work (Richard, 2012; Richard *et al.*, 2012; Richard *et al.*, 2014). We recall here some of the main results.

2.1. Strain in the implanted layer

Four discs of 1 mm thickness were cut from a sintered UO_2 pellet (diameter 8.2 mm). The material is polycrystalline with approximately 18 μm grain size. The discs were implanted with Helium ions at 60 keV energy and fluences varying between 10^{15} and

2.10^{16} ions/cm^2. At this energy, Helium is implanted in a surface layer thiner than $0.4\,\mu$m (see Figure 1). The induced damage, estimated by SRIM software (Ziegler *et al.*, 1985), reaches its maximum at $0.23\,\mu$m depth, and induces a swelling in the implanted layer.

Previous experiments and mechanical modelling have shown that implantation with low energy light ions induces a specific strain field (Richard *et al.*, 2012). It can be described in the sample frame, where z denotes the direction normal to the implanted surface.

- In a first approximation, the displacement gradient $\boldsymbol{\nabla}\xi$ in the implanted layer has only three major components, one normal to the surface $\xi_{z,z}$ and two shear components $\xi_{x,z}$ and $\xi_{y,z}$, depending only on the grain orientation. The six other components $(\xi_{x,x}, \xi_{x,y}, \xi_{y,x}, \xi_{y,y}, \xi_{z,x}, \xi_{z,y})$ are close to zero. The displacement gradient can thus be approximated by:

$$\boldsymbol{\nabla}\xi \approx \begin{pmatrix} 0 & 0 & \xi_{x,z} \\ 0 & 0 & \xi_{y,z} \\ 0 & 0 & \xi_{z,z} \end{pmatrix}. \qquad (1)$$

- A Finite Element mechanical analysis has shown that with a layer thickness much smaller than the average grain size, the previous approximation remains very good: every grain behaves almost independently of the others, with almost uniform strains inside the implanted layer. However the gradient (1) predicted by the simplified model is different in two neighbouring grains, because of their different orientations. This induces a mechanical interaction, particularly important near the grain boundaries.

2.2. Laue pattern with double spots

The principles of ion implantation and X-ray micro-diffraction are presented on Figure 1. The penetration depth of the X-ray beam (about $5\,\mu$m) is much greater than the thickness of the implanted layer (lower than $0.4\,\mu$m). Thus both substrate

and layer in the same grain are probed, with a diffracting volume about ten times bigger in the substrate. A typical Laue pattern, obtained with an incident beam energy range of [5-13 keV], is presented on Figure 2. Each spot is double: a spot of higher intensity (main spot) and a spot of lower intensity (satellite), diffracted respectively by the substrate and the implanted layer. The zoom on a diffraction spot (Figure 3) shows an intense spot for the substrate and another spot for the layer, about 8 times less intense. An accurate examination of the intensity profile shows that the intensity doesn't vanish completely between both spots. This is due to swelling variation along the depth, decreasing between the implanted layer and the substrate.

Since the probed substrate is ten times bigger than the implanted layer, it is almost unaffected by the surface implantation. The corresponding main spots represent a reference state: i.e. the crystal before the implantation. The satellite positions will help to calculate the strain in the implanted layer, relative to the substrate.

2.3. Data collection

Laue X-ray micro-diffraction is used to measure the unit cell strain of a large number of grains. With a polychromatic X-ray beam size (1 μm) much smaller than the UO_2 grain size (18 μm), raster scans are used for two kinds of studies: probing a large number of different grains, or studying intragranular strain variation.

- In the first case, the grid has a large step ($\approx$ 15 μm), similar to the grain size. A collection of about 700 Laue patterns, corresponding to a large number of different grains, has been shown to provide good statistics for evaluating the influence of grain orientation (Richard *et al.*, 2012). A former image analysis failed in analysing some difficult Laue patterns, producing outliers, but this had a low impact on the results due to data redundancy.
- In the second case, the grid has a finer step ($\approx$ 1.5 μm), similar to the beam

size. As the variation of the strain inside a grain is small, it requires higher precision. Furthermore, the mechanical interaction due to incompatible strains in neighbouring grains, important close to the grain boundaries, may alter the spot shapes producing outliers. These outliers must be handled. This implies the development of an accurate image analysis method.

2.4. Strain determination

In a double spot, the 2D pixels position of both the main and satellite spots ($\mathbf{x}_m$ and $\mathbf{x}_s$) correspond to two reciprocal lattice vectors, with the same Miller indices: $\mathbf{K}$ for the non deformed substrate, and $\mathbf{K}'$ in the deformed implanted layer. These vectors are related to each other by the displacement gradient $\nabla\xi$ according to:

$$\mathbf{K}' = (I + \boldsymbol{\nabla}\xi)^{-T}\mathbf{K}, \tag{2}$$

where I denotes the identity matrix. Hence, the relationship between the two spots can be symbolically written as:

$$\mathbf{x}_s = f(\mathbf{x}_m, \boldsymbol{\nabla}\xi). \tag{3}$$

The function f depends on all the geometrical parameters of the experimental setup, which must be determined by a standard calibration procedure.

Therefore, the determination of the gradient $\nabla\xi$ follows three steps:

1. a usual setup calibration and main spots detection,
2. satellite detection,
3. and gradient $\nabla\xi$ determination by solving Equation (3) with a least square procedure.

Two types of information can be deduced from the displacement gradient $\nabla\xi$: the strain ε and rotation ω tensors. For small deformations, as in our case, they can be

obtained as the symmetric and antisymmetric parts of $\nabla\xi$:

$$\nabla\xi = \varepsilon + \omega, \quad \text{with} \quad \varepsilon = \frac{1}{2}(\nabla\xi + \nabla\xi^T), \quad \omega = \frac{1}{2}(\nabla\xi - \nabla\xi^T).$$

The two first steps will be described in Section 3, devoted to image analysis methods, and the last step in Section 4 dealing with least square methods.

3. Digital image processing

3.1. Main spots detection

The first task of a Laue pattern analysis, the main spots detection, has been done using XMAS software (Tamura *et al.*, 2003).

As shown on Figure 3, the main diffraction spots recorded on UO_2 grains can be accurately modelled by 2D Gaussian functions:

$$g(\mathbf{x}_m, a_m, A) = a_m \exp^{-(\mathbf{x}-\mathbf{x}_m)^T.A.(\mathbf{x}-\mathbf{x}_m)}, \tag{4}$$

where $\mathbf{x}_m$ is the spot centre, a_m its amplitude and A a quadratic matrix. Main spots are detected using these Gaussian shape functions. In our Laue patterns, the spot size is about 6 pixels (FWHM about 2 pixels).

3.2. Satellite search

A satellite $\mathbf{x}_s$ is then searched in the neighbourhood of each main spot $\mathbf{x}_m$. This detection is done in two steps: a rough search used to initialise a more accurate one.

In the first step, the image is interpolated by a classical bi-cubic interpolation. A search window is set in the neighbourhood of a main spot $\mathbf{x}_m$. The corresponding satellite $\mathbf{x}_s^r$ is estimated by the local maximum with the highest intensity (excluding the main spot).

In the second step, the satellite positions can be refined by fitting a bi-Gaussian function:

$$b(\mathbf{x}_m, \mathbf{x}_s, a_m, a_s, A) = g(\mathbf{x}_m, a_m, A) + g(\mathbf{x}_s, a_s, A), \tag{5}$$

sum of two Gaussian functions (4), for the main $\mathbf{x}_m$ and satellite $\mathbf{x}_s$ spots, with respective amplitudes a_m and a_s, and a common quadratic matrix A. The bi-Gaussian fit is performed by an iterative least square procedure, which needs a parameter initialisation. For the satellites, the initial values $\mathbf{x}_s^0$ could be the spots $\mathbf{x}_s^r$ found at the first step. But we prefer first to estimate a gradient $\nabla\xi_0$ on these roughly detected satellites $\mathbf{x}_s^r$ (see Section 4). Then the initial values are estimated using Equation (3): $\mathbf{x}_s^0 = f(\mathbf{x}_m, \boldsymbol{\nabla}\xi_0)$. This increases the number of detected satellites, as will be shown in Section 5.

3.3. Satellite detection problems

In some cases, the satellite cannot be detected. There are several reasons to explain this fact:

- The satellite is in average about 8.5 times less intense than the main spot. For low intensity diffraction spots, the satellite disappears in the image background and noise.
- Near the pattern centre, satellites lay close to their main spot, as on Figure 4a, and both spots overlap.
- At grain boundaries, the satellite spot may lose its simple shape, as on Figure 4b: this is due to the mechanical interaction between two or more neighbouring grains, as explained above (Paragraph 2.1).
- At high implantation fluences (2.10^{16} ions/cm^2), plasticity phenomena may appear, transforming the Gaussian shape of the satellite spot, as on Figure 4c, and, in average, the satellite becomes 17 times less intense than the main spot.
- It can also happen that a satellite is found at a bad location, as on Figure 4d due to parasitic spots, belonging to other grains.

3.4. Laue pattern centre

A satellite cannot be detected if it is too close to the main spot: at a distance less than about 2 pixels. In our implanted samples, where the main strain component is $\xi_{z,z}$, normal to sample surface, this situation arises in the centre of the image, and depends slightly on the grain orientation. To illustrate this fact, we have built Figure 5 as follows: given an arbitrary crystal orientation ([3 1 1]), and its corresponding displacement gradient $\boldsymbol{\nabla}\xi$, and using Equation (3), we can map the splitting distance $||\mathbf{x}_m - \mathbf{x}_s||$ between main and satellite spots in Laue pattern. An isoline of 2 pixels, the white circle on the figure, gives approximately the detection limit. For other orientations, it has been found that the circle varies in the area between the red and green circles, corresponding respectively to the [0 0 1] and [1 1 1] orientations.

4. Displacement gradients using least squares method

After the image analysis, the displacement gradient $\boldsymbol{\nabla}\xi$ can be estimated by solving Equation (3) on all the found double spots with a least squares algorithm. Least squares techniques (Draper & Smith, 1981) include also interesting tools, based on statistics, for detecting wrong data and estimating the accuracy of the result. They are described for crystallography by Prince (Prince, 2006).

Since polychromatic Laue diffraction provides the direction of the reciprocal lattice vectors, but not their norm, only the deviatoric part of the displacement gradient can be measured (Chung & Ice, 1999). This leads to a mathematical singularity in the fitting process. To fix it, the displacement gradient is described with only eight non zero components:

$$\boldsymbol{\nabla}\xi \approx \begin{pmatrix} 0 & \xi_{x,y} & \xi_{x,z} \\ \xi_{y,x} & \xi_{y,y} & \xi_{y,z} \\ \xi_{z,x} & \xi_{z,y} & \xi_{z,z} \end{pmatrix}.$$

This is relevant in implanted samples, because the component $\xi_{x,x}$ is close to zero (Richard

et al., 2012).

The least square estimation consists in minimising for each pattern the following cost function:

$$J(\boldsymbol{\nabla}\xi) = \sum_{i=1}^{N} ||\mathbf{x}_{si} - f(\mathbf{x}_{mi}, \boldsymbol{\nabla}\xi)||^2, \tag{6}$$

built on the N found double spots, with function f from Equation 3.

Strain determination from Laue patterns is usually performed on uniformly deformed crystals (Chung & Ice, 1999), where diffraction spots are simple (not double) and cover the entire Laue pattern. In our case, the strain determination is based on the satellite spot positions, and is therefore harder due to the detection difficulties mentioned above: the satellites are fewer, undetectable in the centre of the Laue pattern, and some of them are incorrect. The fitting requires thus a special care.

All statistical tools described below are built on the least square matrix:

$$M = \boldsymbol{\nabla} f^T . \boldsymbol{\nabla} f, \tag{7}$$

where $\boldsymbol{\nabla} f$ denotes the matrix of the derivatives of the function f (Equation 3) with respect to the displacement gradient components. For least squares minimised by a Gauss-Newton algorithm, this matrix is built at each iteration.

4.1. Uncertainty estimation

Least square statistical tools can assess the accuracy of the estimates. The standard deviation of the data noise can be estimated by:

$$\sigma^\star = \sqrt{\frac{1}{N-8} J(\boldsymbol{\nabla}\xi)}, \tag{8}$$

based on the cost function (6) normalised by the degrees of freedom (N-8). This standard deviation is also called goodness-of-fit parameter.

The covariance matrix of the estimated displacement gradient components combines

the least squares matrix (7) and the goodness-of-fit (8):

$$C(\boldsymbol{\nabla}\xi) = \sigma^{\star 2}.M^{-1}.$$

For each component i, the standard deviation error, measuring the estimate accuracy, is:

$$\sigma_i(\boldsymbol{\nabla}\xi) = \sqrt{C_{ii}(\boldsymbol{\nabla}\xi)}.$$

Positioning error The satellite search based on bi-Gaussian fit, described in Paragraph 3.2, needs to be initialised by a first satellite position. This is done by estimating a first gradient $\nabla\xi_0$, and deducing the satellite position using Equation 3: $\mathbf{x}_s^0 = f(\mathbf{x}_m, \boldsymbol{\nabla}\xi_0)$. If the initial guess of the satellite position is too far from the real one, the bi-Gaussian fit will fail to converge to the correct spot.

To avoid this problem, a positioning error can be calculated, based on the covariance matrix of the simulated satellite coordinates:

$$C(\mathbf{x}_s^0) = \boldsymbol{\nabla} f.C(\boldsymbol{\nabla}\xi).\boldsymbol{\nabla} f^T.$$

It is a $2N_0 \times 2N_0$ matrix, for the x and y coordinates of the N_0 main spots. The positioning standard deviation error of the i^{th} estimated satellite is:

$$\sigma_i(\mathbf{x}_s^0) = \sqrt{C_{ii}^x + C_{ii}^y},$$

where C_{ii}^x and C_{ii}^y represent the respective variances for the x and y coordinates. With a spot size of about 6 pixels, it is difficult to find a satellite spot if its initial position lays further than 1 pixel from its real position. After some tests, we decided to eliminate the satellite estimation if its standard deviation $\sigma_i(\mathbf{x}_s^0)$ is greater than 1.25 pixels.

4.2. Conditioning

To fit properly the eight components of the gradient $\boldsymbol{\nabla}\xi$, the couples ($\mathbf{x}_m$,$\mathbf{x}_s$) must cover uniformly the Laue pattern. If an important part of it is empty, the fit may still be possible, but with a bigger uncertainty. The problem becomes ill conditioned: a slight uncertainty on the satellite locations will lead to great perturbations on the displacement gradient.

This may be quantified by the condition number κ, calculated as the ratio of the maximum and minimum eigenvalues of the least square matrix M (Equation 7):

$$\kappa(M) = \frac{\lambda_{\max}}{\lambda_{\min}} \geq 1.$$

This ratio is a coefficient, by which uncertainties are multiplied in solving the least square system. It must be as low as possible. Actually, this coefficient is rarely computed, as it needs to solve a CPU expensive eigenvalues problem. It is instead estimated by the Cholesky algorithm needed to invert the normal Matrix M, as given in any mathematical library. We use SLATEC (Dongarra *et al.*, 1979) for this purpose.

The conditioning problem is illustrated on Figure 6: on a Laue pattern, main spots can be detected everywhere, but the satellite spots can only be detected in the blue region, excluding the pattern centre as explained above. However the estimation is well conditioned with a condition number κ of 500. To simulate a lower quality pattern, with a smaller detection region, we eliminate double spots in the lower part, leaving them only in the green region. Condition number κ raises to 1.4×10^4. Adding to this green region a new satellite in the lower part (red region), reduces it to 2.5×10^3, hence stabilises the gradient fit.

In the best patterns, the condition number κ is about 200. For a series of patterns, the mean condition number is about 600. After a study, we choose $\kappa_L = 10^4$ as a limit to detect ill conditioned patterns and to remove them from the set.

4.3. Influential data points

All data points used in a least square refinement do not have the same weight on the fitted parameters. It is important to detect cases where the fit is controlled by a very few number of points (influential data points). If one of these points is an outlier, it will lead to an incorrect result. Such a case is illustrated in Figure 6, where the satellite in the red zone is isolated: its position cannot be checked by its neighbours. Furthermore, it will have a great influence on the fitted gradient. Such a situation can be identified with the **hat matrix**:

$$H = \boldsymbol{\nabla} f . M^{-1} . \boldsymbol{\nabla} f^T,$$

built on the least square matrix M (Equation (7)) and the model derivatives $\boldsymbol{\nabla} f$. It is a $2N \times 2N$ matrix, where N is the number of double spots contributing in the fit.

The hat matrix is used to evaluate the influence of a double spot on the gradient components estimation. In particular, diagonal terms H^x_{ii} and H^y_{ii} represent the weight of the i^{th} spot coordinates x and y in the gradient fitting, and their sum represents the number of parameters to be fitted:

$$0 \leq H^x_{ii} \leq 1, \quad 0 \leq H^y_{ii} \leq 1 \quad \text{and} \quad \sum_{i=1}^{N} H^x_{ii} + H^y_{ii} = 8.$$

A diagonal element H^x_{ii} or H^y_{ii} close to 1 means that the corresponding coordinate is highly influential on the estimate, *i.e.* has a high leverage score. In the above example (Figure 6), coordinates x and y of the isolated spot have a leverage effect of respectively 0.42 and 0.94.

In an automatic procedure, such satellite might lead to an unreliable fit, as its position could potentially be wrong. In our case a spot is considered as influential if $H^x_{ii} + H^y_{ii} > 1.6$. Removing highly influential spots will of course lead to ill conditioned fit, hence the pattern will be eliminated.

4.4. Detecting incorrect data

As mentioned above, image analysis may provide very uncertain satellite positions if the spots lose their Gaussian shape. In presence of parasitic spots, the location can be completely wrong. Gradient fitting has to deal with these artefacts, *i.e.* to detect and eliminate them. This can be handled by least square statistical tools based on the data redundancy.

Fitting error After the fit, the fitting error can be calculated for each spot:

$$\epsilon = ||\mathbf{x}_s - f(\mathbf{x}_m, \boldsymbol{\nabla}\xi)||, \tag{9}$$

from Equation (3). It represents the distance between the spot measurement and the model supported by all the other spots. It will reach high values for an outlier: a satellite which measured position $\mathbf{x}_s$ lays far from the estimation f obtained by the other satellites.

The uncertainty positioning is about 0.2 pixel for the main and satellite spots. After some tests, we choose a limit of 1 pixel, to consider a satellite position as incorrect. The satellite must be removed from the set and the fit done again.

Goodness-of-fit The goodness-of-fit parameter described above (Equation (8)) estimates the standard deviation of the data noise. It can also check if the strain model (Equation (3)) adequately describes the data. In presence of several artefacts, it will take abnormally high values. For our data, a parameter $\sigma^\star$ greater than 0.5 pixel is considered to indicate an unreliable fit whose result is rejected.

Last two criteria are based on the fitting error (Equation (9)). The first one is local (satellite) and allows to remove the outliers, the second one is global (pattern) and can only eliminate an unreliable fit. These criteria are effective only if other spots lay in the vicinity of an incorrect one.

5. Results

The Laue pattern analysis of He implanted UO_2 samples presented here is based on two features: a bi-Gaussian satellite search and statistical tools provided by least squares. Their efficiency is tested in this section on four samples implanted with Helium at 60 keV with the following fluences: 10^{15}, 5.10^{15}, 10^{16}, and 2.10^{16} ions/cm^2. The X-ray micro-diffraction experiments are performed on BM32 beamline at the European Synchrotron Radiation Facility (Grenoble, France), with a polychromatic X-ray beam of size $\approx 1\times 2$ μm^2 (Ulrich *et al.*, 2011). To each sample corresponds a series of 612 or 816 Laue patterns. The above described methods are implemented in a C++ procedure that can analyse the four series in about 10 minutes.

For these samples, as mentioned in paragraph 2.1, the displacement gradient in the implanted layer has three major components $\xi_{z,z}$, $\xi_{x,z}$ and $\xi_{y,z}$. Their values can reach 1 %, depending on the fluence and the grain orientation. The remaining components have mean and standard deviation close to zero. Their euclidean norm can serve as an indicator of the results quality:

$$||\xi_{\approx 0}|| = \sqrt{\xi_{x,y}^2 + \xi_{y,x}^2 + \xi_{y,y}^2 + \xi_{z,x}^2 + \xi_{z,y}^2}. \tag{10}$$

The efficiency of the new methods and their precision will be evaluated, by calculating for each series the number of successfully analysed images, the mean and maximum values of $||\xi_{\approx 0}||$, denoted respectively by $m(||\xi_{\approx 0}||)$ and $||\xi_{\approx 0}||_{\max}$.

5.1. Improvement using bi-Gaussian shape functions

In Section 3, the spot detection consists of three steps: (1) the main spots detection, (2) a first satellite spots detection by a rough method, (3) a new satellite detection by fitting bi-Gaussian functions. The average numbers of detected diffraction spots are given for each pattern series on Table 1. In each case, the refinement by bi-Gaussian fitting increases the number of detected satellites, because it handles more efficiently

the overlap of satellite and main spots.

In a first analysis, we used the classical Gaussian shape function to detect the satellite spots. Finding the results noisy and wanting to improve their accuracy, we then introduced the bi-Gaussian shape. In order to show the obtained improvement, these two methods are compared on Table 2. The bi-Gaussian fit is always better than the Gaussian fit: the higher number of successful fits indicates a better efficiency, and the lower values of $m(||\xi_{\approx 0}||)$ a more accurate gradient fit.

Compared to the Gaussian, bi-Gaussian functions can detect satellites closer to the main spot. This fact is shown for low fluence (10^{15} ions/cm^2), where the low strain in the implanted layer induces small main spot-satellite distances. In this case, the Gaussian fit fails for almost every collected image.

5.2. Improvement using least square statistical filters

Section 4 described several statistical tools related to least squares, which should improve the gradient fit in presence of badly detected satellites. These tools are filters which detect bad data, and remove them by two ways: in the better case, only a few satellites are removed, improving the gradient fit; in the worst case, the Laue pattern must be removed from the set. The quality of the proposed filters is now tested by switching them on or off, and comparing statistically the results, which are summarised on Table 3.

Using filters eliminates the worst outliers, corresponding to the higher values of $||\xi_{\approx 0}||$, as shown by the reduced maximum value on Table 3. The mean value of $||\xi_{\approx 0}||$ is greater in the absence of filters, but this is mainly due to the outliers elimination. The remaining images have high quality and the results are quite the same with or without filters.

The second and third sets, corresponding to the intermediate fluences, have good

image quality: main spot and satellite are very well separated. Therefore the number of analysed images is reduced only by 2% by the filters. On the other hand, first and last sets are problematic: low implantation fluence induces small main spot-satellite distances, and high implantation fluence deteriorates the Gaussian satellite shape. Finally, 33% and 12% of the images are excluded for the first and fourth sets.

5.3. Local strain mapping

The methods described in this paper are now used to measure strain variation within single grains. For this purpose, a region of $60\times60\,\mu$m has been probed with a $1.5\times2\,\mu$m step on UO_2 polycrystal implanted with 60 keV Helium ions with a fluence of 10^{16} ions/cm^2.

Figure 7 shows the mapped region: each pixel is a result of one Laue pattern analysis. Crystal orientations are first fitted using XMAS software on the main peaks, corresponding to the substrate unaffected by the implantation. The pixel colour code on Figure 7 depends on grain orientation according to a convention described in Appendix A. Grain boundaries are set when orientation difference between two points is greater than 1°. One pixel, crossed out on Figure 7, and located at the intersection of many grains, could not be analysed: the corresponding Laue pattern contains the contribution of too many grains.

Displacement gradients, in the implanted layer, are then estimated using the procedure explained above. Figure 8a, 8b, and 8c show that the components $\xi_{z,z}$, $\xi_{x,z}$, and $\xi_{y,z}$ depend indeed on the grain orientation. According to the simplified model (1), the remaining components $\xi_{\approx0}$ should be close to zero, as if the grains were independent. Their norm $||\xi_{\approx0}||$ (Equation 10), displayed on Figure 8d, confirmed their low values. Their slight increase near the grain boundaries proves the existence of a mechanical interaction between the grains, where the grains can no longer be sup-

posed independent. This interaction causes also a variation of the non-zero components ($\xi_{z,z}$, $\xi_{x,z}$, $\xi_{y,z}$) near the boundaries, which are otherwise homogeneous inside the grains. This short range variation can be attributed to the low penetration depth of 60 keV He ions (0.23 μm in UO_2). For higher implantation energies, hence for deeper implanted layers, mechanical models predict a larger interaction, that will be interesting to investigate.

6. Conclusion

X-ray Micro-diffraction in Laue mode is used to measure the displacement gradient in the deformed layer at the surface of implanted polycrystalline materials. Diffraction spots on Laue patterns are double. A specific image analysis, based on bi-Gaussian shape functions, has been developed to detect accurately the satellites position. It handles better the overlap of main and satellite spots when they are close. This allows a correct analysis of Laue patterns with double spots slightly separated, and improve the accuracy of the strain measurement in all cases. The strain is estimated by a least square procedure, that provides several statistical tools for locating badly detected satellites, and rejecting them. These tools have been used successfully to eliminate unreliable displacement gradients, hence to increase the confidence in the results. The accurate displacement gradient estimation and the reduced number of outliers make it possible to analyse the slight variations of strain field inside the UO_2 grains.

The tools proposed in this paper could also be used to characterise polycrystals whose surface has been either optimised (for example by nitriding (Stinville *et al.*, 2014)) or deteriorated (by corrosion (Chao *et al.*, 2012), oxidation (Desgranges *et al.*, 2010), tribology, polishing or ion beam milling).

References

Barabash, R. I. & Ice, G. E. (eds.) (2014). *Strain and dislocation gradients from diffraction.* Imperial College Press.

Barabash, R. I., Ice, G. E., Liu, W. & Barabash, O. M. (2009). *Micron*, **40**, 28 – 36.

Chao, J., Suominen Fuller, M. L., McIntyre, N. S., Carcea, A. G., Newman, R. C., Kunz, M. & Tamura, N. (2012). *Acta Materialia*, **60**, 781–792.

Chung, J.-S. & Ice, G. (1999). *Journal of Applied Physics*, **86**, 5249–5255.

Desgranges, L., Palancher, H., Gamalri, M., Micha, J. S., Optasanu, V., Raceanu, L., Montesin, T. & Creton, N. (2010). *Journal of Nuclear Materials*, **402**, 167–172.

Dongarra, J. J., Moler, C. B., Bunch, J. R. & Stewart, G., (1979). *LINPACK Users' Guide*. SIAM.

Draper, N. R. & Smith, H. (1981). *Applied Regression Analysis*. Wiley, 2nd ed.

Garcia, P., Martin, G., Desgardin, P., Carlot, G., Sauvage, T., Sabathier, C., Castellier, E., Khodja, H. & Barthe, M.-F. (2012). *J. Nucl. Mater.* **430**, 156–165.

Hauk, V. & Behnken, H. (eds.) (1997). *Structural and Residual Stress Analysis by Nondestructive Methods: Evaluation, Application, Assessment*. Elsevier.

Liu, X., Thadesar, P. A., Taylor, C. L., Oh, H., Kunz, M., Tamura, N., Bakir, M. S. & Sitaraman, S. K. (2014). *Applied Physics Letters*, **105**, 112109.

Marichal, C., Van Swygenhoven, H., Van Petegem, S. & Borca, C. (2013). *Scientific Reports*, **3**, 2547.

Micha, J. S., (2012). Lauetools. Http://sourceforge.net/projects/lauetools/.

Prince, E. (ed.) (2006). *International Tables for Crystallography*, vol. Vol. C, chap. 8 Refinement of structural parameters. Wiley.

Richard, A. (2012). *Etude par diffraction des rayons X des dformations induites par Irradiation/Implantation d'ions dans le dioxyde d'uranium*. Ph.D. thesis, Universite de Poitiers.

Richard, A., Castelier, E., Palancher, H., Micha, J. S., Rouquette, H., Ambard, A., Garcia, P. & Goudeau, P. (2014). *Nucl. Instr. Meth. B*, **326**, 251–255.

Richard, A., Palancher, H., Castelier, E., Micha, J. S., Gamaleri, M., Carlot, G., Rouquette, H., Goudeau, P., Martin, G., Rieutord, F., Piron, J. P. & Garcia, P. (2012). *J. Appl. Cryst.* **45**, 826–833.

Stinville, J., Cormier, J., Templier, C. & Villechaise, P. (2014). *Materials Science and Engineering: A*, **605**, 51 – 58.

Tamura, N., MacDowell, A., Celestre, R., Padmore, H., Valek, B., Bravman, J., Spolenak, R., Brown, W., Marieb, T., Fujimoto, H., Batterman, B. & Patel, J. (2002). *Appl. Phys. Lett.* **80**, 3724–3727.

Tamura, N., MacDowell, A., Spolenak, R., Valek, B., Bravman, J., Brown, W., Celestre, R., Padmore, H., Batterman, B., J.R. & Patel (2003). *Journal of Synchrotron Radiation*, **10**, 137–143.

Ulrich, O., Biquard, X., Bleuet, P., Geaymond, O., Gergaud, P., Micha, J. S., Robach, O. & Rieutord, F. (2011). *Rev. Sci. Instrum.* **82**, 033908.

Villanova, J., Maurice, C., Micha, J.-S., Bleuet, P., Sicardy, O. & Fortunier, R. (2012). *Journal of Applied Crystallography*, **45**, 926–935.

Ziegler, J. F., Biersack, J. P. & Ziegler, M. D., (1985). *SRIM The Stopping and Range of Ions in Matter*. Http://www.srim.org.

Appendix A
Colour and crystal orientation

Crystal orientation can be characterised by three Euler angles, named φ_1, ϕ, φ_2 after Bunge convention (Hauk & Behnken, 1997). The last two angles allow to express the direction **n** normal to the sample surface in the crystal frame, the first angle φ_1 corresponds to an additional rotation around this normal **n**. For a cubic crystal as UO_2, the normal **n** can be displayed in stereographic projections, in the conventional inverse pole representation, in the triangle shown on Figure 9.

A unique colour can be attributed to a crystal using the traditional Hue-Saturation-Value (HSV) colour representation system: Hue, Saturation and Value will correspond respectively to the angles φ_1, φ_2 and ϕ, as on Figure 9.

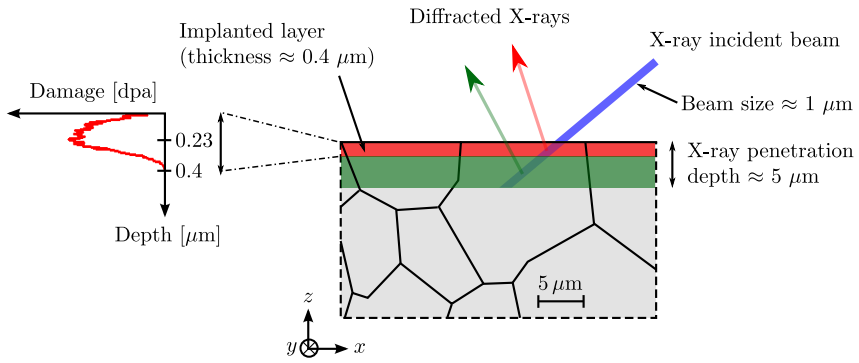


Fig. 1. Schematic representation of a polycrystalline sample implanted in a thin surface layer, marked out in red. The estimated damage profile, due to Helium implantation at 60 keV, is represented along the depth. The X-ray incident beam is diffracted by the damaged layer and the strain free substrate.

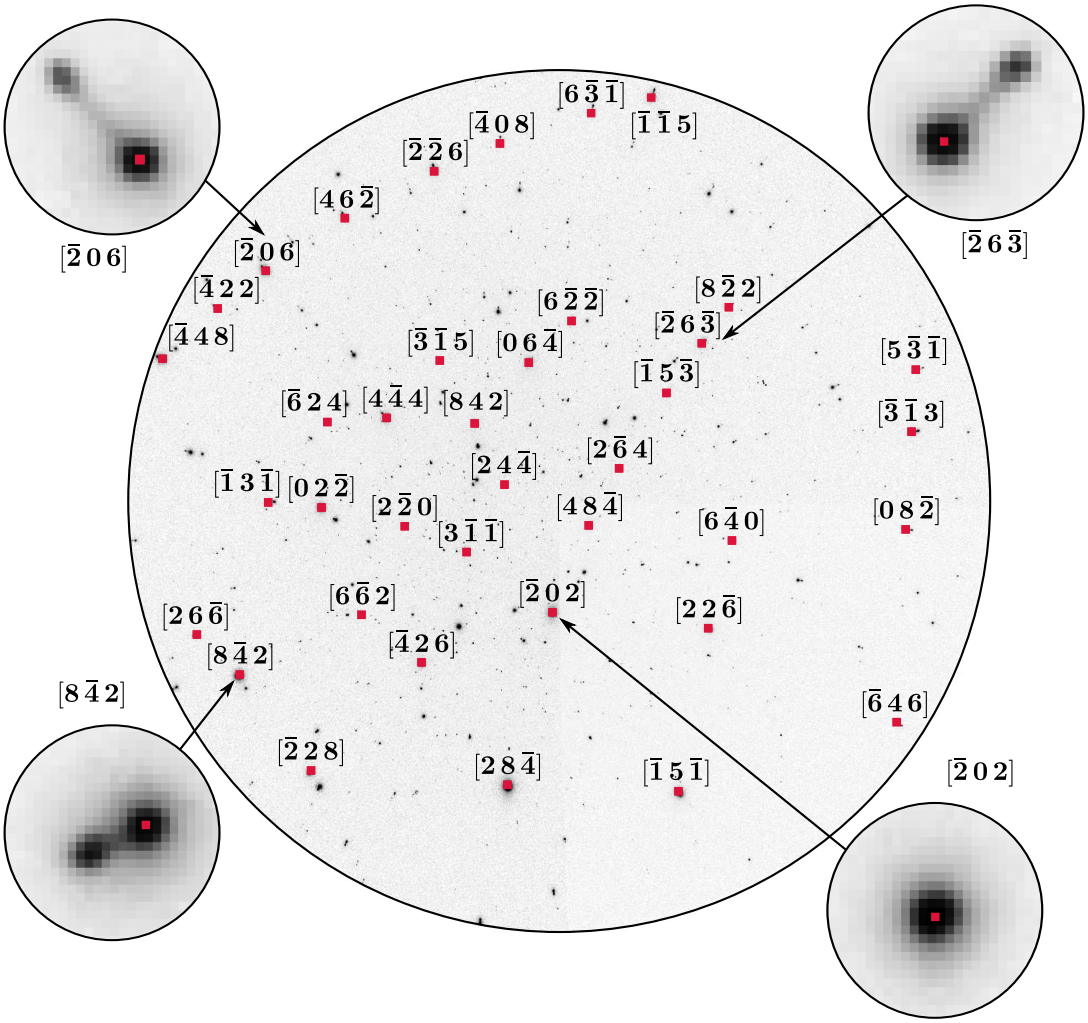


Fig. 2. Laue pattern collected on a Helium implanted UO_2 polycrystal. Strain in the implanted layer causes the splitting of diffraction spots into two components: main spot and satellite. Their distance is minimal in the image centre (see $[\bar{2}02]$ Bragg reflection), and maximal near the image borders (see $[\bar{2}06]$,$[\bar{2}6\bar{3}]$ Bragg reflections). From one Laue pattern, the crystal orientation and the strain in the implanted layer can be measured.

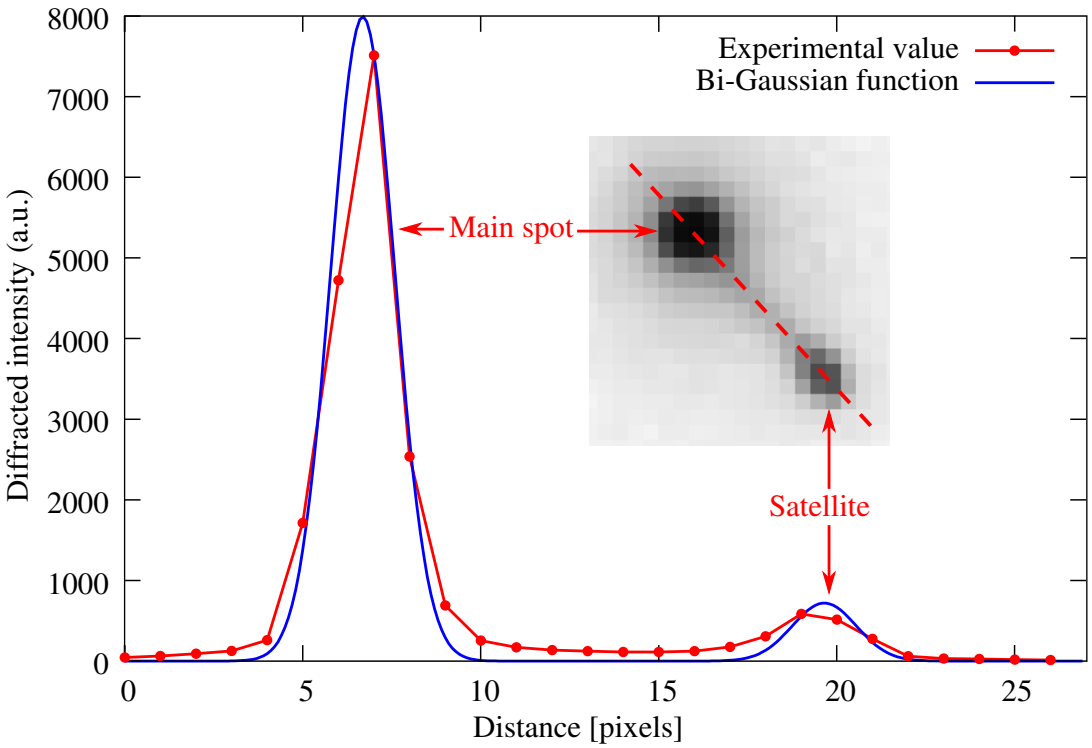


Fig. 3. Example of diffracted intensity profile measured between a main spot and its associated satellite. This profile has been interpolated along the red dashed line between both spots shown on the zoom. A bi-Gaussian function is fitted on the experimental values.

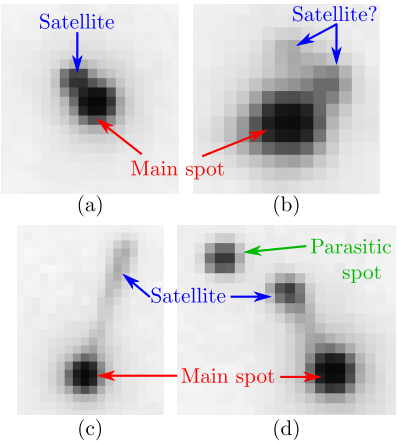


Fig. 4. Four cases of difficult satellite detection in Laue pattern measured on He-implanted UO_2 polycrystals: (a) satellite close to the main spot; (b) complicated satellite shape near the grain boundaries; (c) elongated satellite for high implantation fluence; (d) presence of a parasitic spot.

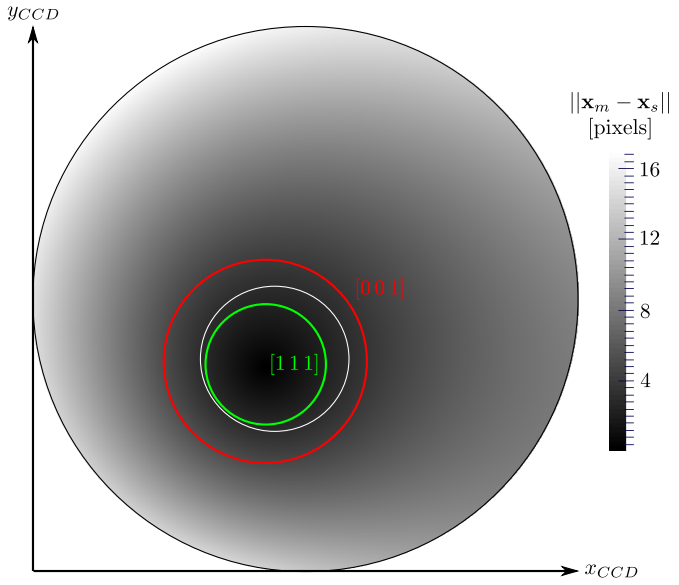


Fig. 5. Map on the CCD detector of the satellite/main spot distance for a [3 1 1] oriented grain. The white circle indicates a satellite/main peak distance of 2 pixels. The same isoline has been also drawn in green and red for [0 0 1] and [1 1 1] oriented grains respectively.

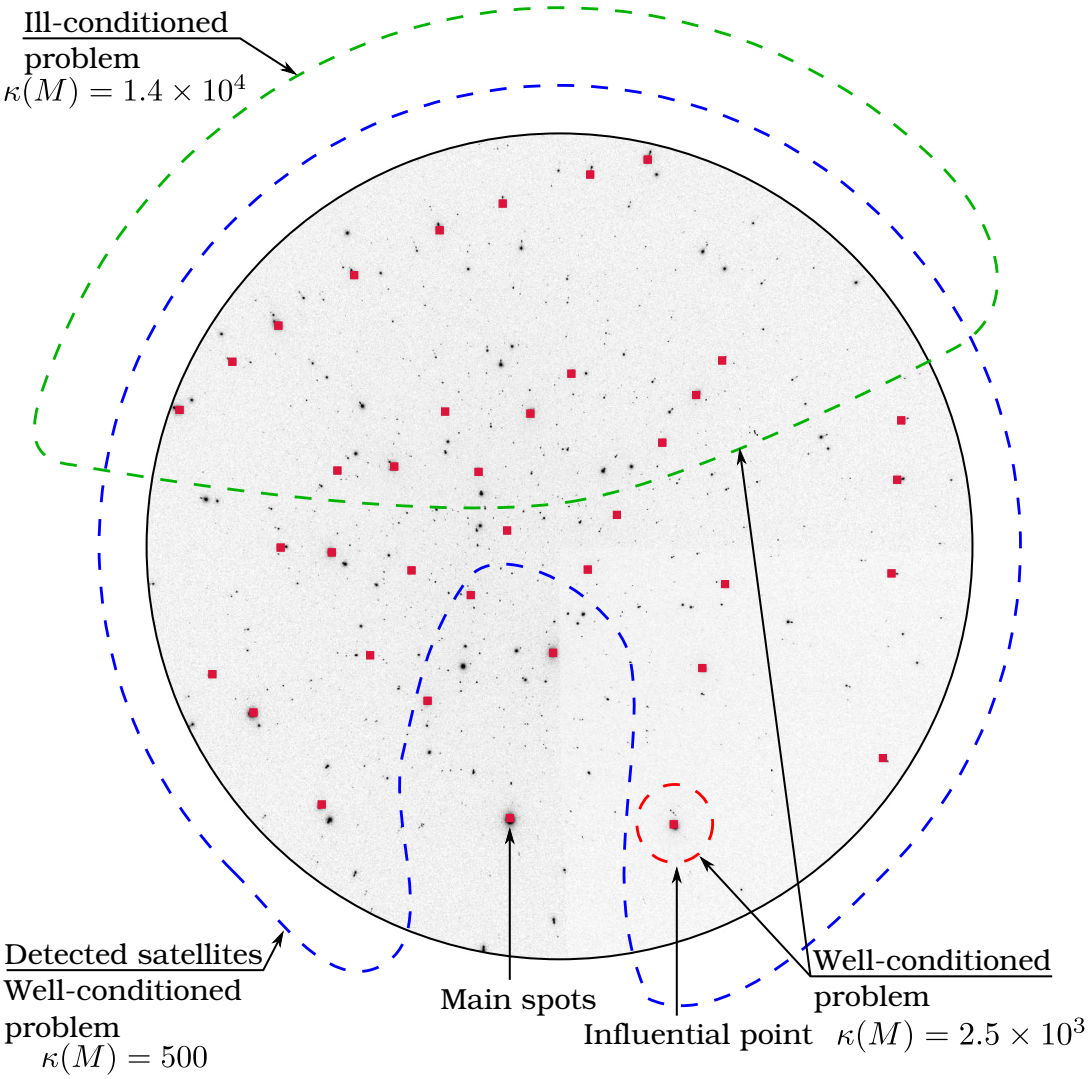


Fig. 6. Illustration of the conditioning problem on a Laue pattern. Three regions are marked out: blue and green regions lead respectively to a well and ill-conditioned case. Adding a point (red circle) to the green region is enough to make the problem well-conditioned.

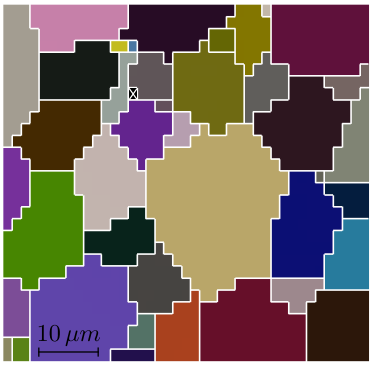


Fig. 7. Grain orientation mapping of the strain-free substrate, calculated on the main spots for a UO_2 polycrystal implanted with 60 keV Helium ions at 10^{16} ions/cm^2. The corresponding colours follow HSV convention described in Appendix A.

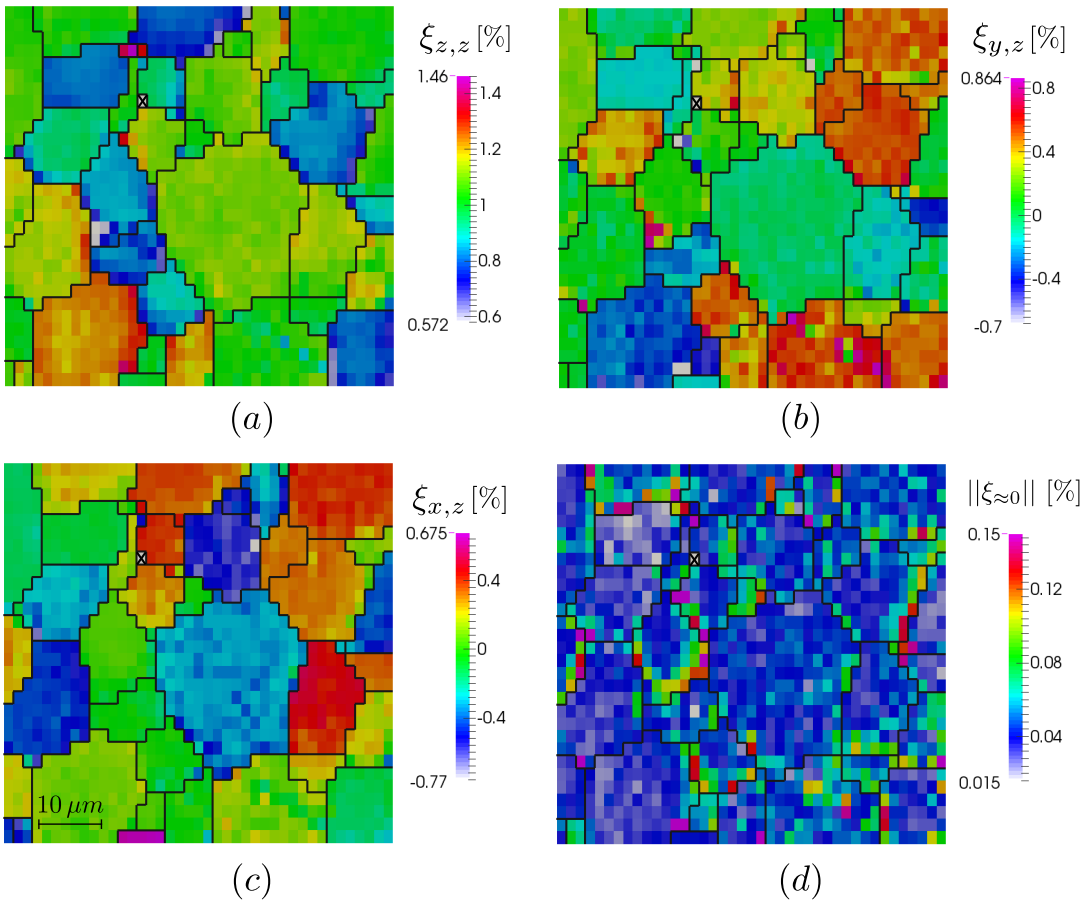


Fig. 8. Displacement gradient mapping in the implanted layer calculated on the double spots for a UO_2 polycrystal implanted with 60 keV Helium ions at 10^{16} ions/cm^2. Maps (a), (b), (c) and (d) display respectively the components $\xi_{z,z}$, $\xi_{y,z}$, $\xi_{x,z}$ and the euclidean norm of the remaining components. The corresponding grain orientations are displayed on Figure 7.

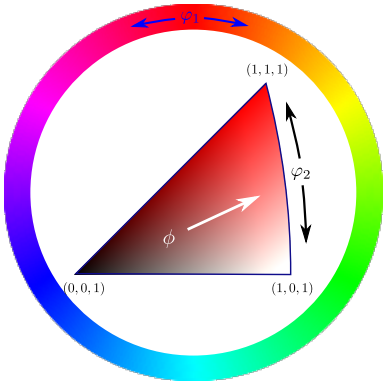


Fig. 9. Hue-Saturation-Value (HSV) colour coding for cubic crystal orientation: Hue, Saturation and Value correspond to the traditional Bunge angles φ_1, φ_2 and ϕ.

Table 1. *In a Laue pattern, the satellite spots are searched close to main spots, firstly by a rough method, secondly by fitting bi-Gaussian functions. For each pattern series, the mean number of detected main spots is given, as well as the mean number of detected satellites by both methods.*

Fluences [ions/cm^2]	Mean number of detected spots per Laue pattern		
	Main spots	Rough detection	bi-Gaussian
10^{15}	23.6	11.6	19.8
5.10^{15}	23.9	17.4	22.4
10^{16}	27.1	18.8	25.5
2.10^{16}	23.8	16.6	22.5

Table 2. *Comparison of the satellite fitting methods, using the classical Gaussian or the bi-Gaussian shapes, on the pattern sets corresponding to the four fluences. Number of successfully analysed patterns and mean value of* $||\xi_{\approx 0}||$.

Fluences [ions/cm^2]	Number of patterns	Successfully analysed patterns		$m(\|\|\xi_{\approx 0}\|\|)$ [%]	
		Gaussian	bi-Gaussian	Gaussian	bi-Gaussian
10^{15}	612	14	587	0.069	0.033
5.10^{15}	612	367	594	0.055	0.031
10^{16}	816	647	811	0.052	0.033
2.10^{16}	816	663	808	0.098	0.092

Table 3. *Effect of the filters on the series corresponding to the four fluences: number of successfully analysed patterns, mean and maximum values of* $||\xi_{\approx 0}||$.

Fluences [ions/cm^2]	Number of patterns	Successfully analysed patterns		$m(\|\|\xi_{\approx 0}\|\|)$ [%]		$\|\|\xi_{\approx 0}\|\|_{\max}$ [%]	
		Filters		Filters		Filters	
		OFF	ON	OFF	ON	OFF	ON
10^{15}	612	587	380	0.033	0.026	0.612	0.114
5.10^{15}	612	594	576	0.031	0.023	2.257	0.214
10^{16}	816	811	801	0.033	0.031	0.574	0.375
2.10^{16}	816	808	716	0.092	0.088	1.741	0.503